Journal of Molecular Liquids xxx (xxxx) 120383

Contents lists available at ScienceDirect

Journal of Molecular Liquids

journal homepage: www.elsevier.com/locate/molliq

Hydrogen bonding of nanoconfined water in ionic liquids

Hiroshi Abe *, Yuto Yoshiichi, Takaaki Hirano, Taichi Ohkubo, Hiroaki Kishimura

Department of Materials Science and Engineering, National Defense Academy, Yokosuka 239-8686, Japan

ARTICLE INFO

Article history:
Received 18 July 2022
Received in revised form 3 September 2022
Accepted 12 September 2022

Keywords:
Water pocket
Ionic liquids
Hydrogen bonding
H/D exchange
Water-in-salt
pD

ABSTRACT

1-Alkyl-3-methylimidazolium nitrate ([$C_n$mim][NO_3], n = 4, 6, and 8)-D_2O was provided a small-angle neutron scattering (SANS) peak, representing D_2O aggregations (Abe *et al.*, *J. Phys. Chem. Lett.* 5 (2014) 1175 and *J. Mol. Liq.* 346 (2022) 117035). Nanoconfined water (water pocket) appeared in the water-rich region, with a size distribution that was almost monodispersed. The water pocket in [C_4mim][NO_3] was characterized by the hydrogen bonding (Abe *et al.*, *J. Mol. Liq.* 210 (2015) 200). In this work, the hydrogen bonding state of [$C_n$mim][NO_3]-D_2O (n = 2, 6, and 8) that was examined by Raman spectroscopy, the water concentration dependencies of the OD stretching band of D_2O indicated that the hydrogen bonding state of the water pocket was invariant. The hydrogen/deuteron (H/D) exchange reaction was observed only in [C_6mim][NO_3]-D_2O, with the H/D exchange completed within 1 h. Moreover, large pD values were observed only in [C_6mim][NO_3]-D_2O, and the kinetic pD behavior supported the H/D exchange.

1. Introduction

Nanoconfined water is investigated in various research fields [1–3]. It is formed in solids such as graphene sheets [4–8], carbon nanotubes [9–11], and nanoporous silica [12–15]. While the properties of nanoconfined water are influenced by hydrophilic or hydrophobic walls, the structures, dynamics, and hydrogen bonding states of nanoconfined water are different from those of bulk water. In contrast, water is loosely confined on the nanoscale, even in liquid circumstances. Where specifically, in a water-poor region, water-in-salt distinctly appears and contributes to stable high-voltage aqueous Li-ion batteries [16], aqueous solutions cause water aggregations in a specific water concentration [15–19].

Ionic liquids (ILs) are multi-functional liquids that can be freely designed for each application by changing the cation–anion combination [20]. ILs possess nanoheterogeneous liquid structures [21,22]. A representative cation is 1-alkyl-3-methylimidazolium, [$C_n$mim]$^+$, where n reveals the alkyl chain length. The polar and nonpolar nanodomain sizes are tuned by the alkyl chain length. As nanoenvironments, ILs are studied with respect to the local stiffness and softness of nanodomains [23].

Water confinement in ILs has attracted considerable attention among research communities. The nanoheterogeneity of [C_8mim][NO_3]–H_2O was examined by molecular dynamics simulations [24]. Near the boundaries of the polar and nonpolar nanodomains, nanoconfined water or "water pocket" was formed, even in a liquid state. Accordingly, small-angle neutron scattering (SANS) experiments were conducted to observe the water pocket. Experimental results showed that a SANS peak appeared in [$C_n$mim][NO_3]-D_2O (n = 4, 6, and 8) [25–27], illustrating that a water pocket was spontaneously formed in the water-rich region. The size of the water pocket in [C_4mim][NO_3] was estimated to be 2 nm. This water pocket helped explain the partially globular state of a double-sized lysozyme [28]. The water concentration dependence of Raman bands in [C_4mim][NO_3]-D_2O was also observed [29,30]. In contrast to that of bulk water, the hydrogen bonding strength was weakened at 70–90 mol% D_2O, whose concentration region was characterized by the water pocket existence. In addition, when [C_4mim][NO_3]-D_2O was used, the slow dynamics of water was probed by quasielastic neutron scattering (QENS) [31]. A slow proton transfer was also observed in tiny nanodroplets through polarization-resolved fluorescence-IR spectroscopy [32], where, compared with the QENS of bulk water, the bulk water-like fast dynamics was not induced in the water pocket. The water pocket is described by its small size, monodispersive distribution, weak hydrogen bonding, and slow dynamics. The water pocket at room temperature contributed to the solidifications at low temperature. At 70–90 mol% D_2O, the crystallizations of both [C_4mim][NO_3] and D_2O are suppressed completely [33]. The water pocket in ILs is summarized in the literature [34,35], Where, in addition to the water pocket, the hydrogen/deuteron (H/D) exchange reaction is also observed in hydrophilic [$C_n$mim][X]-D_2O by NMR and Raman spectroscopy [36–41]. By adding D_2O, H linked to the

* Corresponding author.
E-mail address: ab@nda.ac.jp (H. Abe).

https://doi.org/10.1016/j.molliq.2022.120383
0167-7322/© 20XX

second carbon, C(2), of $[C_n mim]^+$ (Fig. 1(a)) can be easily replaced with D in imidazolium-based ILs. The alkyl chain length of cation and anion determines its reaction kinetics. Hydrophobic IL-2-propanol-d_8 indicates the H/D exchange [42]. The IL is 1-alkyl-3-methylimidazolium bis(trifluoromethanesulfonyl)imide, $[C_n mim][TFSI]$ (n = 2–6). The H/D exchange lacks alkyl chain length dependence.

In this study, we investigate the hydrogen bonding states of $[C_n mim][NO_3]$-D_2O (n = 2, 6, and 8) through Raman spectroscopy, where H/D exchange is observed only in $[C_6 mim][NO_3]$-D_2O. The water pocket is spontaneously formed when $n \geq 4$. Where a specific hydrogen bonding different from that of bulk water is developed in the water pocket, the hydrogen bonding states in $[C_n mim][NO_3]$-D_2O are drastically changed with or without the water pocket. The pD values support the H/D exchange only in $[C_6 mim][NO_3]$-D_2O.

2. Experimental method

$[C_2 mim][NO_3]$ (>98.0 %) was received from Tokyo Chemical Industry, Co. and a solid at room temperature. The $[C_6 mim][NO_3]$ and $[C_8 mim][NO_3]$ liquids (>98.0 %) at room temperature were purchased from Angene Chemical, Co. We used the as-received samples after vacuum drying for a few days. Distilled D_2O (99.9 %, Merck Co.) was then selected. The hydrophilic IL and D_2O mixture was prepared inside a glove box under flowing helium gas to avoid atmospheric moisture. The samples were mixed through 100 times of hand shaking, considering that the molecules are easily damaged in an ultrasonic bath. The sample treatment was the same as that in a previous study [27]. In the kinetic experiments, we started to count time just after mixing in the dry box. [42].

An NRS-5100 Raman spectrometer (JASCO Co.) equipped with a monochromator and a Peltier-cooled camera was used for the measurements. Excitation was triggered by a 5.8 mW green laser with 532 nm wavelength. We measured Raman spectra of each sample three times:

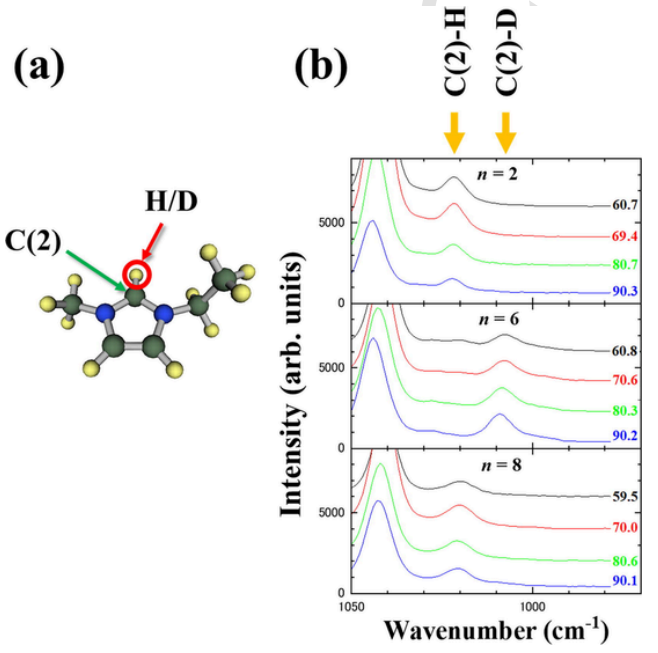

Fig. 1. (a) Molecular structure of $[C_2 mim]^+$ and atomic position of C(2). (b) Raman intensities of $[C_n mim][NO_3]$-x mol% D_2O (n = 2, 6, and 8). The data were collected after 2 days of mixing. The numbers in the figure reveal the water concentrations. H/D exchange on the Raman bands. The 1010 and 1024 cm^{-1} Raman bands corresponded to C(2)-D and C(2)-H, respectively. The numbers in the figure reveal x mol% D_2O.

1 h, 2 day, and 4 months after mixing. Fully equilibrated mixtures were stored at room temperature for 4 months.

A semiconductor pH sensor (ISFET 0040-10D, Horiba Co.) was used for the pH measurements. The pH values were calibrated using the following standard pH solutions: $KH_3(C_2O_4)_2{\cdot}2H_2O$ (pH = 1.68), C_6H_4(COOK)(COOH) (pH = 4.01), KH_2PO_4 + Na_2HPO_4 (pH = 6.86) (Horiba Co.), and $Na_2B_4O_7 10H_2O$ (pH = 9.18). The semiconductor pH meter was placed in a metal container continuously flushed with helium gas to reduce the atmospheric moisture [43]. Inside the container, the pH sensor was immersed in the sample.

3. Computational details

Density functional theory (DFT) calculations were performed to optimize the molecular structures of $[C_n mim][NO_3]$ (n = 2, 4, 6, and 8) and the molecular complex of $[NO_3]^-$ and $m(H_2O)$ (m = 0, 1, 2, and 3). Furthermore, the molecular conformations of the $[C_n mim]^+$ cations were assessed energetically. The Raman bands were obtained by DFT. A scaling factor of 0.964 was used for the Raman bands. All DFT calculations were performed using the B3LYP hybrid functional and the 6–31++G(d,p) basis set of the *Firefly* package [44,45].

4. Results and discussion

4.1. H/D exchange of $[C_6 mim][NO_3]$-D_2O

$[C_4 mim][NO_3]$-D_2O indicated no H/D exchange over the whole water concentration range [41]. Even after 58 days, the H/D exchange was not induced in $[C_4 mim][NO_3]$-D_2O [30]. The H/D exchange generally occurred at the second carbon C(2)-H of the $[C_n mim]^+$ cation (Fig. 1(a)). The H/D exchange rate was determined by two Raman bands: 1010 cm^{-1} of C(2)-D and 1024 cm^{-1} of C(2)-H [40,41]. These Raman bands were defined as a result of the combination of the in-plane ring and CH_3(N) deformations. The mode is illustrated in Fig. S1. Fig. 1(b) presents the Raman bands of the H/D exchange of fully equilibrated $[C_n mim][NO_3]$-D_2O (n = 2, 6, and 8). In $[C_2 mim][NO_3]$-D_2O, the Raman band representing C(2)-H existed at concentrations >50 mol% D_2O (Fig. 1(b)). No C(2)-D was present in the $[C_2 mim][NO_3]$-based system; therefore, no H/D exchange occurred in $[C_2 mim][NO_3]$-D_2O even when the D_2O concentration was varied. The models for the HOD-mediated hydrogen bonding were considered based on the hydrogen bond formation free energy [46].

$[C_6 mim][NO_3]$-D_2O provided entirely opposing behaviors for the H/D exchange. Instead, of C(2)-H at 1024 cm^{-1}, an obvious C(2)-D Raman band was located at 1010 cm^{-1} (Fig. 1(b)). Above 50 mol% D_2O, this tendency with C(2)-D and without C(2)-H did not change. With this result, the complete H/D exchange occurred in $[C_6 mim][NO_3]$-D_2O. Fig. 2 depicts an in-situ observation of the H/D exchange reaction in $[C_6 mim][NO_3]$-82.0 mol%. The C(2)-H Raman band was gradually reduced, whereas the C(2)-D intensity inversely developed. In a significant finding for the kinetic H/D exchange, time dependent the H/D exchange provides slow dynamics of the deuteron replacement. The anion effect of the H/D exchange was previously investigated [40,41].

$[C_8 mim][NO_3]$ with a longer alkyl chain was examined to determine whether or not the chain length would affect the H/D exchange effect. From the distinct C(2)-H Raman band without C(2)-D, $[C_8 mim][NO_3]$-D_2O showed no H/D exchange (Fig. 1(b)). The H/D exchange was again prohibited in $[C_8 mim][NO_3]$. While the C(2)-H stretching could be different among the various samples, but the H/D exchange was not observed in either $[C_2 mim][NO_3]$- or $[C_8 mim][NO_3]$-D_2O, where, compared with the peak width of the Raman band of $[C_2 mim][NO_3]$-D_2O, the broader Raman band of C(2)-H was dominant in $[C_8 mim][NO_3]$-D_2O.

Consequently, the H/D exchange was only activated in $[C_6 mim][NO_3]$ via the D_2O additive. One of the possible reasons for this

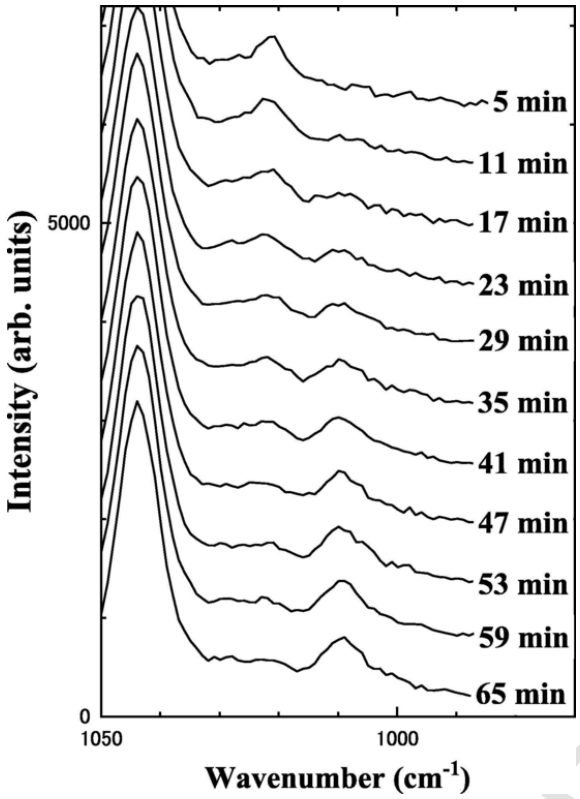

Fig. 2. Time dependence of Raman intensity in $[C_6mim][NO_3]$-82.0 mol% D_2O. Kinetic H/D exchange appeared at room temperature. The numbers in the figure reveal time after mixing the samples.

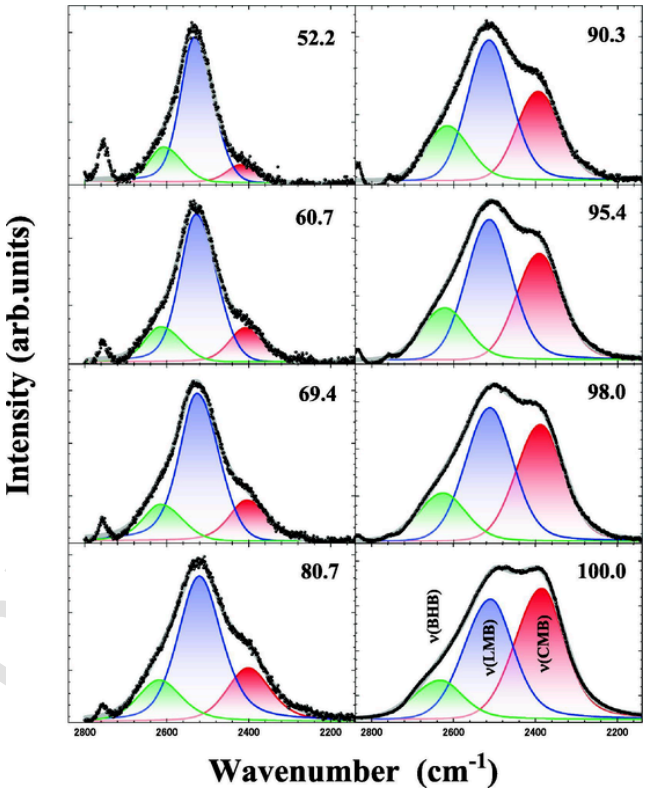

Fig. 3. D_2O Raman bands in $[C_2mim][NO_3]$-x mol% D_2O. The number in the figure reveals the D_2O concentrations. The CMB, LMB, and BHB reveal weak hydrogen-, medium hydrogen-, and strong hydrogen-bonded water, respectively.

is the degrees of freedom of the $[C_nmim]^+$ conformers [47–49]. $[C_2mim]^+$ had planar (p) and non-planar (n), while the stable conformers of $[C_4mim]^+$ were calculated as ntt, ngt, ng't, and ng'g' [48]. Here, *trans*, *gauche*, and *gauche*' are denoted by t, g, and g', respectively. In the case of $[C_6mim]^+$, 15 stable conformers were assessed [48]. By DFT, $[C_8mim]^+$ revealed three conformations, namely, nttttt, ngttttt, and ng'ttttt [49]. Fig. S2 presents the optimized conformations of $[C_nmim]^+$ (n = 4, 6, and 8). $[PFBS]^-$ was perfluorobutanesulfonate where, experimentally, the crystal polymorphs of $[C_nmim][PFBS]$ (n = 4, 6, and 8) were observed at low temperature [50]. The cationic conformations for each crystal were assigned via Raman spectroscopy [51]. Experimentally, in the crystal states of $[C_8mim][PFBS]$, nttttttt, ntgtttt, and ntg'tttt conformers were observed at low temperature [51]. In a liquid state, the broad band of *trans*-like conformers was formed at room temperature. Therefore, in $[C_8mim]^+$, alkyl chain packing could be preferred with excluding the *gauche*-like conformers. In conclusion, several $[C_6mim]^+$ conformations might trigger the H/D exchange. The protein system's structural flexibility aided in the H/D exchange [52].

4.2. D_2O Raman bands in $[C_nmim][NO_3]$ (n = 2, 6, and 8)-D_2O

The OH and OD stretching bands of bulk water were investigated by Raman spectroscopy associated with the hydrogen bonding network [53,54]. The asymmetric band profile was derived from two hydrogen bonding components [53]. The OH stretching Raman band of the bulk water was interpreted using intra- and intermolecular coupling [54]. The 3250 cm^{-1}, 3490 cm^{-1}, and 3650 cm^{-1} Raman bands were identified as a collective mode, local mode, and broken hydrogen bond, respectively. The hydrogen bonding state of the HOD was experimentally and conceptually examined [55].

$[C_2mim][NO_3]$-D_2O had no water pocket, as evidenced by the absence of a SANS peak [27]. No nanoheterogeneity occurred in the pure $[C_2mim][NO_3]$. Fig. 3 illustrates the OD stretching bands of D_2O in $[C_2mim][NO_3]$-x mol% D_2O. The Raman bands were decomposed into three parts using the asymmetric pseudo-Voigt function [29]. The observed OD stretching Raman bands were assigned as collective mode band (CMB) at 2390 cm^{-1}, local mode band (LMB) at 2520 cm^{-1}, and broken hydrogen bond band (BHB) at 2620 cm^{-1}. The intensity fraction of the Raman bands is given as follows:

$$f_i = \frac{I_i}{I_{CMB} + I_{LMB} + I_{BHB}}, \quad (1)$$

where I_{CMB}, I_{LMB}, and I_{BMB} reveal the intensities of the CMB, LMB, and BHB Raman bands, respectively. The intensities were obtained using the fitted peak intensities and widths. In Fig. S3, the intensity fractions, f_i, of the Raman bands are plotted on the water concentration scale. In pure D_2O, the largest Raman band was CMB. Once the IL was dissolved into D_2O, the CMB gradually decreased with the increasing IL content (Fig. S3). This tendency was similar to $[C_4mim][NO_3]$-D_2O [29,30]. A monotonic decrease of the CMB and a monotonic increase of the LMB simultaneously occurred with the decreasing water concentration. The water pocket was not formed in $[C_2mim][NO_3]$-D_2O: hence, the bent curves of f_i were not observed above 50 mol%. A constant f_i appeared between 60 and 87 mol% due to the water pocket in the case of $[C_4mim][NO_3]$-D_2O [30]. In $[C_2mim][NO_3]$-D_2O, the hydrogen bonding of D_2O did not change discreetly on the water concentration scale. No drastic Raman band shifts of CMB, LMB, and BHB were observed with changing water concentration.

In the $[C_6mim][NO_3]$-D_2O system, a distinct SANS peak appeared at 70–90 mol% [27]. An almost monodispersive water pocket was also spontaneously formed. NMR previously showed that HOD water was formed by the H/D exchange in $[C_4mim][BF_4]$-D_2O [38]. In $[C_6mim][NO_3]$-D_2O, the H/D exchange effect should be considered for the Raman intensities (Fig. 2). In contrast to f_i of $[C_2mim][NO_3]$-D_2O,

$[C_6mim][NO_3]$ changed the water concentration dependency of f_i (Fig. S3). At 90–100 mol% without a water pocket, the CMB, LMB, and BHB of $[C_6mim][NO_3]$-D_2O in Fig. 4 were the same as those of $[C_2mim][NO_3]$-D_2O. In the absence of a water pocket above 90 mol% in both systems, the hydrogen bonding of percolated water was equivalent between both. Below 80 mol%, f_{BHB} drastically decreased and disappeared below 60 mol%. Moreover, the CMB shifted to a lower wavenumber (redshift) with a decreasing water concentration. The H/D exchange occurred in $[C_6mim][NO_3]$-D_2O; thus, the HOD effect should be considered in addition to D_2O. In the previous study [55], the BHB of the bulk HOD indicated a blueshift, while the strong hydrogen bond was characterized by a redshift. The hydrogen bonding of D_2O was not modified by the $[C_2mim]^+$ and $[NO_3]^-$ species, with the HOD population growing with the decreasing water concentration; hence, the CMB redshift of the water pocket (Fig. 4) was identical to that of bulk water. However, the observed redshift of the BHB was unclear.

$[C_8mim][NO_3]$-D_2O showed the "water pocket" in the water-rich region [27] without the H/D exchange (Fig. 1(b)). Therefore, the hydrogen bonding state of the water pocket without the HOD was extracted via Raman spectroscopy, where the water pocket existed at 70–90 mol%. Fig. 5 reveals the CMB, LMB, and BHB of $[C_8mim][NO_3]$-D_2O. The same water concentration dependence of f_i was obtained at 95–100 mol%. Fig. S3 shows that the f_i values of $[C_2mim][NO_3]$-, $[C_6mim][NO_3]$-, and $[C_8mim][NO_3]$-D_2O coincide with each other. However, discrete f_i changes were detected only in $[C_8mim][NO_3]$-D_2O at 90 mol%. Furthermore, almost constant f_{CMB}, f_{LMB}, and f_{BHB} values were obtained at 70–90 mol%. This constant intensity fraction was also found in $[C_4mim][NO_3]$-D_2O [30].

In other words, the water pocket existence governs the hydrogen bonding state, and the hydrogen bonding state inside the water pocket is not influenced by the water concentration at 70–90 mol%. With the significant point is that CMB disappearing at 50 mol% (Fig. 5), we also stress here that the hydrogen bonding state of the water pocket differs from that of bulk water due to the different f_i values. The nanoheterogeneity was well developed in the pure $[C_8mim][NO_3]$ with a long alkyl chain. Water could be isolated, and a hydrogen bonding network could not form, in the water-poor region.

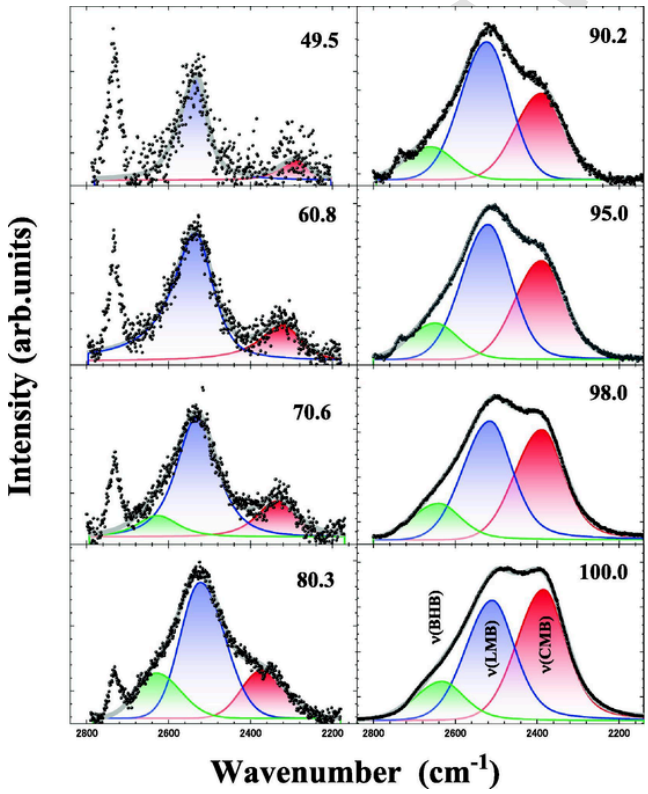

Fig. 4. D_2O Raman bands in $[C_6mim][NO_3]$-x mol% D_2O. The number in the figure reveals the D_2O concentrations.

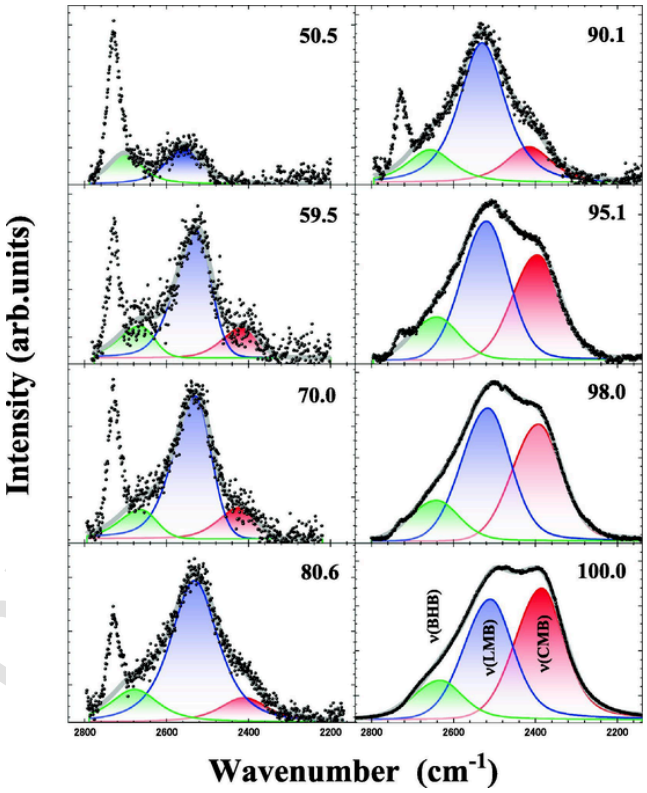

Fig. 5. D_2O Raman bands in $[C_8mim][NO_3]$-x mol% D_2O. The number in the figure reveals the D_2O concentrations.

4.3. DFT calculations of the $[NO_3]^-$ Raman bands

In Raman spectroscopy, the $[NO_3]^-$ stretching and bending modes were obtained in $[C_4mim][NO_3]$-D_2O [30]. Where in particular, in the bending mode, the Raman bands were sensitive to the local environments [56], the Raman band at 1041 cm^{-1} was assigned to the $[NO_3]^-$ stretching mode, and the 706 cm^{-1} peak was identified as the $[NO_3]^-$ bending mode. The symmetry breaking of $[NO_3]^-$ was induced by the water hydrogen bonding. The nitrate hydration at ~720 cm^{-1} and the contact ion pairing at ~740 cm^{-1} of different kinds of nitrate aqueous solutions were analyzed via Raman spectroscopy [57]. Hydration and ion pairing were differentiated by the Raman band at ~710 cm^{-1}. The DFT calculations could support the possibility of water-in-salt related to the water pocket.

We next investigated the effect of hydrated nitrate ion by calculating the Raman bands of the $[NO_3]^-$-$m(H_2O)$ complex using DFT. Where the contact ion pairing effect was evaluated with cations and $[NO_3]^-$ without water molecules, in Fig. S4, a gradual blueshift was obtained both in the stretching and bending modes with the increasing numbers of water molecules. The alkyl chain length effect for the $[NO_3]^-$ stretching and bending modes was also calculated using pure $[C_nmim][NO_3]$ (n = 2, 4, 6, and 8) (Fig. S5). From n = 2 to n = 6, the blueshift was dominant in the stretching mode, but $[C_8mim][NO_3]$ did not indicate a blueshift. The blueshift could not occur proportionally to the alkyl chain length (Fig. S5). We next focused on the calculated bending mode. The bending mode of $[NO_3]^-$ indicated no blueshift even when the alkyl chain length was changed. However, the band splitting was calculated in $[C_nmim][NO_3]$. For instance, the triplet Raman bands of the bending mode appeared only in $[C_2mim][NO_3]$. This is a significant feature of the Raman bands for $[NO_3]^-$.

4.4. $[NO_3]^-$ Raman bands of $[C_nmim][NO_3]$-D_2O

Fig. 6 depicts the $[NO_3]^-$ stretching and bending modes in $[C_2mim][NO_3]$-D_2O. The stretching mode at 1041 cm^{-1} shifted to a higher Raman wavenumber with the increasing water concentration. The blueshift of the stretching mode was supported by DFT (Fig. S4). The bending Raman band of $[C_2mim][NO_3]$-60.7 mol% D_2O was located in the center of 705 cm^{-1}, which was similar to that of $[C_4mim][NO_3]$-60 mol% D_2O [30]. In $[C_4mim][NO_3]$-D_2O, the bending mode comprised two Raman bands attributed to nitrate hydration (700 cm^{-1}) and ion pairing (710 cm^{-1}). The 700 cm^{-1} band of $[C_4mim][NO_3]$-D_2O was positioned at the fixed wavenumber, although the 710 cm^{-1} band shifted to a higher wavenumber above 50 mol% D_2O [30]. This bending mode tendency was discovered in $[C_2mim][NO_3]$-D_2O (Fig. 6). More interestingly, nitrate hydration in $[C_2mim][NO_3]$-D_2O existed, even at 95.4 mol% D_2O. The DFT calculations (Fig. S5) showed that the blueshift of the bending bands was derived from an increase in the coordination number of the water molecules bounded to the $[NO_3]^-$ anion. The invariant positioning of the nitrate hydration suggested that the water coordination number is almost constant. Alternatively, the blueshift of the ion pairing band implied that the cation and anion interaction was sensitive to the water content. Whereas in the local conditions in both systems not being dependent on the formation or nonformation of the water pocket in the water-rich region, here, similar water concentration dependencies of $[C_2mim][NO_3]$- and $[C_4mim][NO_3]$-D_2O were obtained.

Fig. 7 presents the observed Raman bands of the $[NO_3]^-$ anion in the $[C_6mim][NO_3]$-D_2O system. The Raman shifts with respect to the water concentration were not compared with the other systems because of the H/D exchange only in the $[C_6mim][NO_3]$-based system. The HOD water derived from the H/D exchange contributes differently to the Raman bands of the $[NO_3]^-$ anion. Thus, we cannot directly compare the Raman shifts with the other IL-based systems having no H/D exchange. A blueshift was observed in the $[C_6mim][NO_3]$-D_2O system.

$[C_8mim][NO_3]$-D_2O is a prototype of the hydrogen bonding state that is directly associated with the water pocket. The SANS peak of the $[C_8mim][NO_3]$-based system suggests that the water pocket exists without the H/D exchange [27]. Direct comparisons of $[C_2mim][NO_3]$- and $[C_8mim][NO_3]$-D_2O can clarify the influence of the water pocket on the $[NO_3]^-$ anion because both systems showed no H/D exchange (i.e., no HOD water). This is a significant experimental fact for addressing the specific hydrogen bonding of the water pocket. The stretching Raman bands of $[C_8mim][NO_3]$-D_2O provided a continuous blueshift with the increasing water concentration in the same manner as $[C_2mim][NO_3]$- and $[C_6mim][NO_3]$-D_2O (Fig. 8). Fig. S6 illustrates the blueshifts as a function of the water concentration. A notable difference is that the stretching Raman band of $[C_8mim][NO_3]$-D_2O changed to a lower wavenumber when compared to the stretching mode of $[C_2mim][NO_3]$-D_2O. The DFT calculations in Fig. S4 showed that he blueshift was caused by water hydrations. Consequently, water

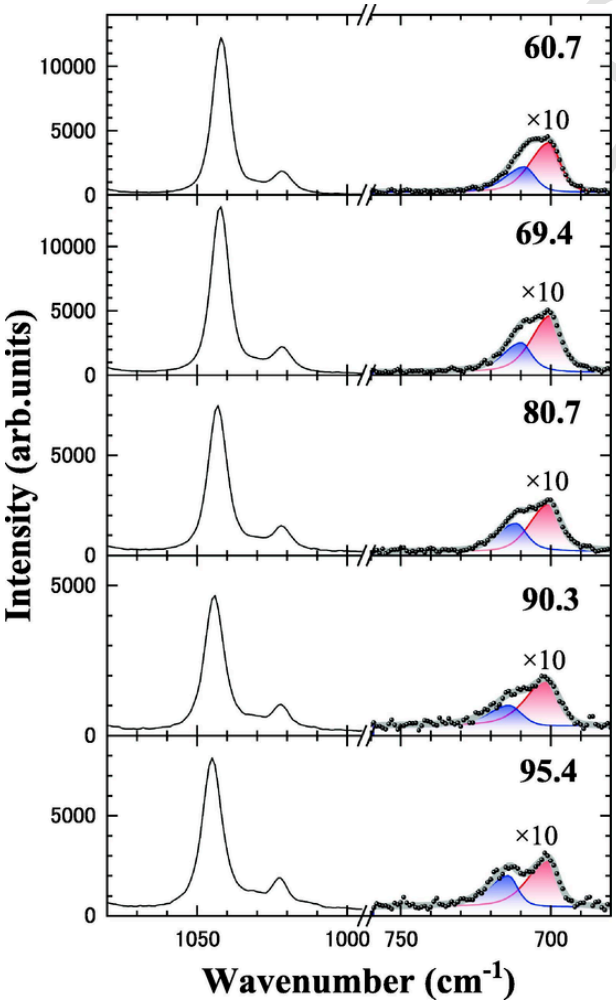

Fig. 6. $[NO_3]^-$ anion symmetric stretching mode at 1041 cm^{-1} and bending mode at 706 cm^{-1} of $[C_2mim][NO_3]$-D_2O. The number in the figure reveal the D_2O concentrations.

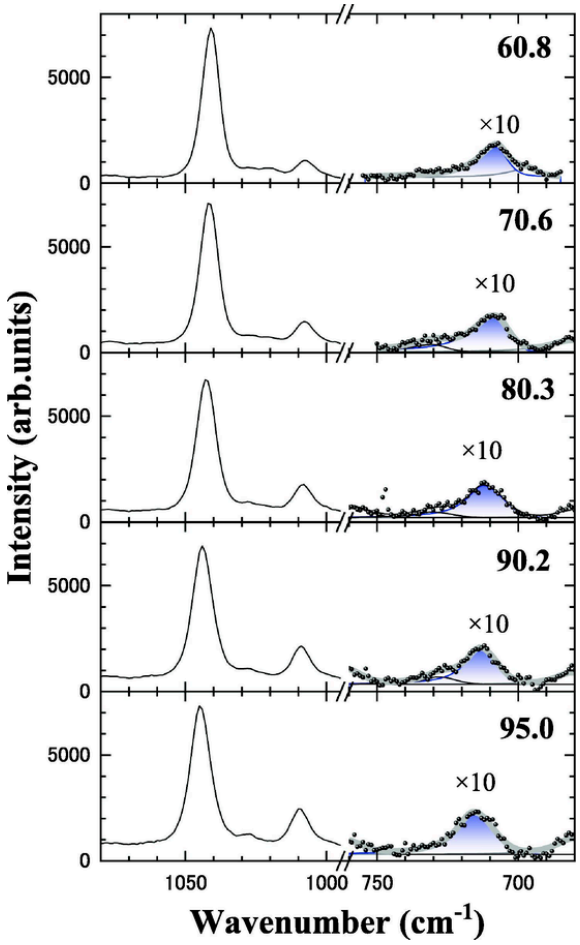

Fig. 7. $[NO_3]^-$ anion symmetric stretching and bending modes at 1041 cm^{-1} and 706 cm^{-1}, respectively, of $[C_6mim][NO_3]$-D_2O. The number in the figure reveals the D_2O concentrations.

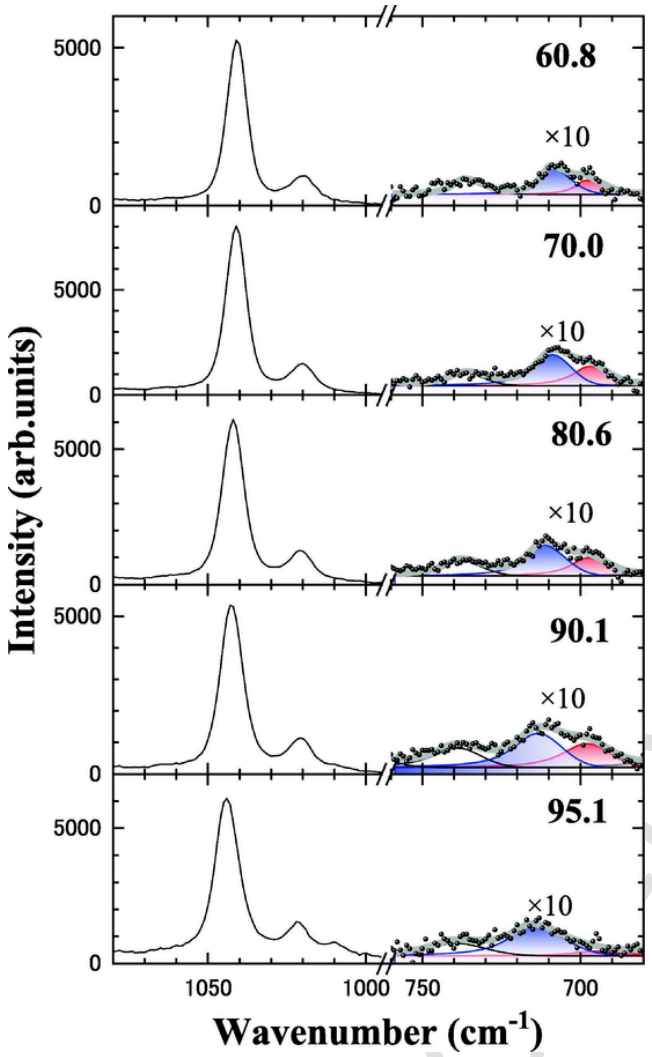

Fig. 8. $[NO_3]^-$ anion symmetric stretching and bending modes at 1041 cm^{-1} and 706 cm^{-1}, respectively, of $[C_8mim][NO_3]$-D_2O. The number in the figure reveals the D_2O concentrations.

hydration was extensively promoted in $[C_2mim][NO_3]$-D_2O. These hydration behaviors were also discovered in the bending mode. Apparently, in $[C_8mim][NO_3]$-D_2O, the Raman intensity of the ion pairing at 710 cm^{-1} was larger than that of nitrate hydration at 700 cm^{-1}. Furthermore, at 95.1 mol% D_2O, the hydration band of $[C_8mim][NO_3]$-D_2O nearly vanished (Fig. 8), with the intensity ratio of $[C_8mim][NO_3]$-D_2O opposing that of $[C_2mim][NO_3]$-D_2O. As a result, a weak nitrate hydration was observed in $[C_8mim][NO_3]$-D_2O.

Table 1 summarizes the water pocket properties. The water pocket appeared at $4 \le n$ and developed with the increasing n. The intensity fraction, f_i, of the OD stretching mode became constant at $70 \le x \le 90$ mol% D_2O. The hydrogen bonding state in the water pocket could not be influenced by the abovementioned concentration. Nevertheless, in $[C_6mim][NO_3]$-D_2O, we cannot calculate the f_i due to the H/D exchange effect. The 700 cm^{-1} Raman band representing the nitrate hydration clarified the difference between $[C_4mim][NO_3]$- and $[C_8mim][NO_3]$-D_2O. In the $[C_8mim][NO_3]$-based system, a large water pocket and a weak nitrate hydration were characterized. Hence, the ion pairing of the cation and the anion was preferred in the large water pocket ($70 \le x \le 90$ mol%). The size of the water pocket and the hydration state might be altered by varying the alkyl chain length. A key discovery in this study sheds fresh light on the use of water pockets in water-in-salt applications.

Table 1
Properties of the water pocket in $[C_nmim][NO_3]$ (n = 2, 4, 6, and 8).

$[C_2mim]^+$	$[C_2mim]^+$	$[C_4mim]^+$	$[C_6mim]^+$	$[C_8mim]^+$
H/D exchange	×	×	○	×
Size of water pocket (nm)	–	~1.8	~2.8	~3.3
f_i ($70 \le x \le 90$) D_2O	Variant	Constant	–	Constant
Nitrate hydrationanion	Strong	Strong	–	Weak
pD	7–8	6.4–7.4	8.9–9.5	6.8–7.9

4.5. pD of $[C_nmim][NO_3]$-D_2O

The H/D exchange was connected with the pD values [58,59]. Here, pD was obtained as follows [60]:

$$pD = pH + 0.40 \quad (2)$$

The exchange rate constants were represented by a V-shaped curve on the pD scale. The V-shaped curves were changed by molecular conformers, ionic strength, and temperature. The H/D exchange was also monitored through the pD measurements. In the protein system [58], the C(2) imidazole protons were influenced by geometrical accessibility to the protons. The H/D exchange was accelerated when the C(2) protons were exposed to D_2O.

Fig. 9 presents the water concentration dependence of pD in $[C_nmim][NO_3]$ (n = 2, 4, 6, and 8). The samples were fully equilibrated because of 60-day storage at room temperature. In $[C_2mim][NO_3]$-x mol% D_2O, the neutral pD slightly increased with the increasing D_2O concentration. D_2O was well dissolved into $[C_2mim]^+$ without the water pocket formation and could be mobile between $[C_2mim]^+$ and $[NO_3]^-$. A neutral pD implied that D_2O cannot stay only in $[C_2mim]^+$. The $[C_8mim][NO_3]$-D_2O system also provided a monotonic pD increment of (Fig. 9). In the case of $[C_8mim][NO_3]$-D_2O, a distinct water pocket was formed [27], appearing near the nanodomain boundaries in the simulation box [24]. Thus, D_2O could be excluded from the C(2)-H position. In contrast, different pD tendencies were observed in $[C_4mim][NO_3]$-D_2O. The pD value was minimized at approximately 85 mol% D_2O. The concentration region coincided with that of the water pocket existence in $[C_4mim][NO_3]$-D_2O. Therefore, the water pocket might contribute to the H/D exchange suppression. More importantly, the pD of $[C_6mim][NO_3]$-D_2O became nearly 9 (Fig. 9). In the previous studies [58,59], the exchange rate constants extensively increased on the alkali side. The time dependence of pD in $[C_6mim][NO_3]$-80 mol% D_2O was measured to compare the time evo-

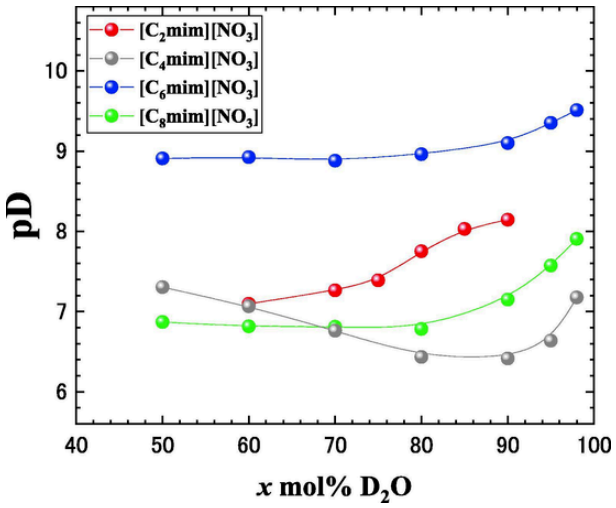

Fig. 9. Water concentration dependences of $[C_nmim][NO_3]$-D_2O (n = 2, 4, 6, and 8).

lutions of the Raman bands in Fig. 2. The pD value saturated within 1 h (Fig. S7), indicating that the observed pD corresponded to the H/D exchange. The H/D exchange in $[C_6mim][NO_3]$-D_2O was certified by the time-resolved Raman spectroscopy and the pD measurements. Accessibility to the C(2) proton was deduced to be enhanced by flexibility and many degrees of freedom of $[C_6mim]^+$ [48].

5. Conclusions

In this work, the hydrogen bonding states of $[C_nmim][NO_3]$ (n = 2, 6, and 8) were examined by Raman spectroscopy with respect to nanoconfined water, also known as water pocket. Anomalous H/D exchanges were induced only in $[C_6mim][NO_3]$-D_2O. The anomaly was connected with large pD values only in $[C_6mim][NO_3]$-D_2O. The alkyl chain length-dependent H/D exchange was first observed herein. $[C_2mim][NO_3]$-D_2O was characterized by absence of both an H/D exchange and water pocket, while $[C_8mim][NO_3]$-D_2O was represented by the lack of both H/D exchange and a water pocket at 70–90 mol%. The water pocket-driven hydrogen bonding was directly obtained by comparing $[C_8mim][NO_3]$-D_2O with $[C_2mim][NO_3]$-D_2O. The hydrogen bonding state of the water pocket did not change at 70–90 mol%. The intensity fractions of the CMB, LMB, and BHB were different from those of bulk water. A weak nitrate hydration was observed in $[C_8mim][NO_3]$-D_2O. In conclusion, various kinds of water pocket in ILs are useful for the water-in-salt technology.

CRediT authorship contribution statement

Hiroshi Abe : Conceptualization, Writing – original draft, Writing – review & editing. **Yuto Yoshiichi :** Data curation, Formal analysis. **Takaaki Hirano :** Data curation. **Taichi Ohkubo :** Data curation. **Hiroaki Kishimura :** Data curation.

Declaration of Competing Interest

The authors declare that they have no known competing financial interests or personal relationships that could have appeared to influence the work reported in this paper.

Data availability

The authors do not have permission to share data.

Acknowledgments

We thank Dr. T. Takekiyo and Professor Y. Yoshimura of the National Defense Academy and Professor A. Shimizu of Soka University for helpful discussions.

Appendix A. Supplementary material

Supplementary data to this article can be found online at https://doi.org/10.1016/j.molliq.2022.120383.

References

[1] G. Fraux, F.-X. Coudert, A. Boutin, A.H. Fuchs, Forced intrusion of water and aqueous solutions in microporous materials: from fundamental thermodynamics to energy storage devices, Chem. Soc. Rev. 46 (2017) 7421–7437.
[2] D. Muñoz-Santiburcio, D. Marx, Chemistry in nanoconfined water, Chem. Sci. 8 (5) (2017) 3444–3452.
[3] M. Foroutana, S.M. Fatemi, F. Esmaeilian, A review of the structure and dynamics of nanoconfined water and ionic liquids via molecular dynamics simulation, Eur. Phys. J. E 40 (2017) 11507–11517.
[4] Z. Gao, N.S. Giovambattista, O. Sahin, Phase diagram of water confined by graphene, Sci. Rep. 8 (2018) 6228.
[5] S. Varghese, S.K. Kannam, J.S. Hansen, S.P. Sathian, Effect of hydrogen bonds on the dielectric properties of interfacial water, Langmuir 35 (2019) 8159–8166.
[6] L. Shi, A. Xu, D. Pan, T. Zhao, Aqueous proton-selective conduction across two-dimensional graphyne, Nature Commun. 10 (2019) 1165–1168.
[7] F. Jiménez-Ángeles, K.J. Harmon, T. Dac Nguyen, P. Fenter, M.O. de la Cruz, Nonreciprocal interactions induced by water in confinement, Phys. Rev. Reas. 2 (2020) 043244.
[8] F. Leoni, C. Calero, G. Franzese, Nanoconfined fluids: uniqueness of water compared to other liquids, ACS Nano 15 (2021) 19864–19876.
[9] K.V. Agrawal, S. Shimizu, L.W. Drahushuk, D. Kilcoyne, M.S. Strano, Observation of extreme phase transition temperatures of water confined inside isolated carbon nanotubes, Nat. Nanotech. 12 (2017) 267–274.
[10] X. Ma, S. Cambré, W. Wenseleers, S.K. Doorn, H. Htoon, Quasiphase transition in a single file of water molecules encapsulated in (6,5) carbon nanotubes observed by temperature-dependent photoluminescence spectroscopy, Phys. Rev. Lett. 118 (2017) 027402-7.
[11] K. Otake, K. Otsubo, T. Komatsu, S. Dekura, J.M. Taylor, R. Ikeda, K. Sugimoto, A. Fujiwara, C.-P. Chou, A.W. Sakti, Y. Nishimura, H. Nakai, H. Kitagawa, Confined water-mediated high proton conduction in hydrophobic channel of a synthetic nanotube, Nat. Commun. 11 (2020) 843–847.
[12] R. Renou, A. Szymczyk, A. Ghoufi, Water confinement in nanoporous silica materials, J. Chem. Phys. 140 (2014) 044704-8.
[13] A.W. Knight, N.G. Kalugin, E. Coker, A.G. Ilgen, Water properties under nano-scale confinement, Sci. Rep. 9 (2019) 8246–8312.
[14] S.A. Yamada, J.Y. Shin, W.H. Thompson, M.D. Faye, Water dynamics in nanoporous silica: ultrafast vibrational spectroscopy and molecular dynamics simulations, J. Phys. Chem. C 123 (2019) 5790–5803.
[15] H. Zhu, F. Yang, Y. Zhu, A. Li, W. He, J. Huang, G. Li, Investigation of dielectric constants of water in a nano-confined pore, RSC Adv. 10 (15) (2020) 8628–8635.
[16] L. Suo, O. Borodin, T. Gao, M. Olguin, J. Ho, X. Fan, C. Luo, C. Wang, K. Xu, Water-in-salt electrolyte enables high-voltage aqueous lithium-ion chemistries, Science 350 (6263) (2015) 938–943.
[17] A. Serva, N. Dubouis, A. Grimaud, M. Salanne, Confining water in ionic and organic solvents to tune its adsorption and reactivity at electrified interfaces, Acc. Chem. Res. 54 (2021) 1034–1042.
[18] N.C. Osti, B.P. Thapaliya, S. Dai, M. Tyagi, E. Mamontov, Strong enhancement of nanoconfined water mobility by a structure breaking salt, J. Phys. Chem. Lett. 12 (2021) 4038–4044.
[19] H.R. Corti, G.A. Appignanesi, M.C. Barbosa, J.R. Bordin, C. Calero, G. Camisasca, M.D. Elola, G. Franzese, P. Gallo, A. Hassanali, K. Huang, D. Laria, C.A. Meńendez, J.M. Montes de Oca, M.P. Longinotti, J. Rodriguez, M. Rovere, D. Scherlis, I. Szleifer, Structure and dynamics of nanoconfined water and aqueous solutions, Eur. Phys. J. E 44 (2021) 136–150.
[20] F. Philippi, T. Welton, Targeted modifications in ionic liquids – from understanding to design, Phys. Chem. Chem. Phys. 23 (12) (2021) 6993–7021.
[21] J.N.A. Canongia Lopes, A.A.H. Pádua, Nanostructural organization in ionic liquids, J. Phys. Chem. B 110 (2006) 3330–3335.
[22] A. Triolo, O. Russina, H.-J. Bleif, E. Di Cola, Nanoscale segregation in room temperature ionic liquids, J. Phys. Chem. B 111 (18) (2007) 4641–4644.
[23] R.P. Daly, J.C. Araque, C.J. Margulis, Communication: stiff and soft nano-environments and the "*Octopus Effect*" are the crux of ionic liquid structural and dynamical heterogeneity, J. Chem. Phys. 147 (2017) 061102-05.
[24] W. Jiang, Y. Wang, G.A. Voth, Molecular dynamics simulation of nanostructural organization in ionic liquid/water mixtures, J. Phys. Chem. B 111 (2007) 4812–4818.
[25] H. Abe, T. Takekiyo, M. Shigemi, Y. Yoshimura, S. Tsuge, T. Hanasaki, K. Ohishi, S. Takata, J. Suzuki, Direct evidence of confined water in room-temperature ionic liquids by complementary use of small-angle X-ray and neutron scattering, J. Phys. Chem. Lett. 5 (2014) 1175–1180.
[26] H. Abe, T. Takekiyo, M. Shigemi, Y. Yoshimura, S. Tsuge, T. Hanasaki, K. Ohishi, S. Takata, J. Suzuki, Size-tunable confined water in a room temperature ionic liquid, JPS Conf. Proc. 8 (2015) 033001-6.
[27] H. Abe, F. Nemoto, K. Hiroi, K. Ohishi, S. Takata, Spontaneous formations of nanoconfined water in ionic liquids by small angle neutron scattering, J. Mol. Liq. 346 (2022) 117035–117036.
[28] T. Takekiyo, K. Yamazaki, E. Yamaguchi, H. Abe, Y. Yoshimura, High ionic liquid concentration-induced structural change of protein in aqueous solution: a case study of lysozyme, J. Phys. Chem. B 116 (36) (2012) 11092–11097.
[29] H. Abe, T. Takekiyo, M. Aono, H. Kishimura, Y. Yoshimura, N. Hamaya, Polymorphs in room-temperature ionic liquids: hierarchical structure, confined water and pressure-induced frustration, J. Mol. Liq. 210 (2015) 200–214.
[30] J. Kausteklis, M. Talaikis, V. Aleksa, V. Balevičius, Raman spectroscopy study of water confinement in ionic liquid 1-butyl-3-methylimidzolium nitrate, J. Mol. Liq. 271 (2018) 747–755.
[31] H. Abe, T. Yamada, K. Shibata, Dynamic properties of nano-confined water in an ionic liquid, J. Mol. Liq. 264 (2018) 54–57.
[32] O.O. Sofronov, H.J. Bakker, Slow proton transfer in nanoconfined water, ACS Cent. Sci. 6 (2020) 1150–1158.
[33] H. Abe, T. Takekiyo, Y. Yoshimura, K. Saihara, A. Shimizu, Anomalous freezing of nano-confined water in room-temperature ionic liquid 1-butyl-3-methylimidazolium nitrate, ChemPhysChem 17 (8) (2016) 1136–1142.
[34] H. Abe, T. Takekiyo, Y. Yoshimura, A. Shimizu, Static and dynamic properties of nano-confined water in room-temperature ionic liquids, J. Mol. Liq. 290 (2019) 111216–111219.
[35] H. Abe, Phase variety in ionic liquids: hydrogen bonding and molecular conformations, J. Mol. Liq. 332 (2021) 115189–115227.
[36] A.A. Shahkhatuni, A.G. Shahkhatuni, V.P. Ananikov, A.S. Harutyunyan, NMR-monitoring of H/D exchange reaction of ketones in solutions of imidazolium ionic liquids, J. Mol. Liq. 362 (2022) 119746–119748.

[37] Y. Yasaka, C. Wakai, N. Matubayasi, M. Nakahara, Slowdown of H/D exchange reaction rate and water dynamics in ionic liquids: deactivation of solitary water solvated by small anions in 1-butyl-3-methyl-imidazolium chloride, J. Phys. Chem. A 111 (2007) 541–543.
[38] S. Ohta, A. Shimizu, Y. Imai, H. Abe, N. Hatano, Y. Yoshimura, Peculiar concentration dependence of H/D exchange reaction in 1-butyl-3-methylimidazolium tetrafluoroborate-D_2O mixtures, Open J. Phys. Chem. 1 (2011) 70–76.
[39] N. Hatano, M. Watanabe, T. Takekiyo, H. Abe, Y. Yoshimura, Anomalous conformational change in 1-butyl-3-methylimidazolium tetrafluoroborate–D_2O mixtures, J. Phys. Chem. A 116 (2012) 1208–1212.
[40] V. Klimavicius, Z. Gdaniec, J. Kausteklis, V. Aleksa, K. Aidas, V. Balevicius, NMR and Raman spectroscopy monitoring of proton/deuteron exchange in aqueous solutions of ionic liquids forming hydrogen bond: a role of anions, self-aggregation, and mesophase formation, J. Phys. Chem. B 117 (2013) 10211–10220.
[41] Y. Yoshimura, N. Hatano, T. Takekiyo, H. Abe, Direct correlation between the H/D exchange reaction and conformational changes of the cation in imidazolium-based Ionic liquid–D_2O mixtures, J. Sol. Chem. 43 (9–10) (2014) 1509–1518.
[42] H. Abe, Y. Yoshiichi, H. Kishimura, Hydrogen/deuterium exchange in 1-alkyl-3-methylimidazolium bis(trifluoromethanesulfonyl)imide-based solutions, Chem. Phys. 562 (2022) 111631–111637.
[43] H. Abe, K. Nakama, R. Hayashi, M. Aono, T. Takekiyo, Y. Yoshimura, K. Saihara, A. Shimizu, Electrochemical anomalies of protic ionic liquid – water systems: a case study using ethylammonium nitrate – Water system, Chem. Phys. 475 (2016) 119–125.
[44] A.A. Granovsky, Firefly version 8, Available from: <www.http://classic.chem.msu.su/gran/firefly/index.html>.
[45] M.W. Schmidt, K.K. Baldridge, J.A. Boatz, S.T. Elbert, M.S. Gordon, J.H. Jensen, S. Koseki, N. Matsunaga, K.A. Nguyen, S. Su, T.L. Windus, M. Dupuis, J.A. Montgomery Jr, General atomic and molecular electronic structure system, J. Comput. Chem. 14 (1993) 1347–1363.
[46] P.A. Sigala, E.A. Ruben, C.W. Liu, P.M.B. Piccoli, E.G. Hohenstein, T.J. Martínez, A.J. Schultz, D. Herschlag, Determination of hydrogen bond structure in water versus aprotic environments to test the relationship between length and stability, J. Am. Chem. Soc. 137 (2015) 5730–5740.
[47] J.N. Canongia Lopes, J. Deschamps, A.A.H. Pádua, Modeling ionic liquids using a systematic all-atom force field, J. Phys. Chem. B 108 (2004) 2038–2047.
[48] T. Endo, T. Higuchi, Y. Kimura, DFT study on conformation of 1-alkyl-3-methylimidazolium with ethyl, propyl, butyl, pentyl, and hexyl group, Bull. Chem. Soc. Jpn. 93 (6) (2020) 720–729.
[49] S. Bilgili, F. Bardak, E. Kose, A. Atac, Investigation of the interionic interactions and spectroscopic features of 1-Octyl-3-methylimidazolium chloride, tetrafluoroborate, and hexafluorophosphate ionic liquids: an experimental survey and DFT modeling, J. Mol. Str. 1261 (2022) 132912–132914.
[50] Y. Koyama, S. Shimono, H. Abe, K. Matsuishi, Crystal polymorphs in 1-alkyl-3-methylimidazolium perfluorobutanesulfonate ionic liquids, J. Mol. Liq. 317 (2020) 113908–113917.
[51] H. Abe, H. Kishimura, M. Uruichi, A phase variety of fluorinated ionic liquids: molecular conformational and crystal polymorphs, submitted to Spectrochim. Acta.
[52] P. Zavodszky, J. Kardos, A. Svingor, G.A. Petsko, Adjustment of conformational flexibility is a key event in the thermal adaptation of proteins, Proc. Natl. Acad. Sci. 95 (1998) 7406–7411.
[53] J.D. Smith, C.D. Cappa, K.R. Wilson, R.C. Cohen, P.L. Geissler, R.J. Saykally, Unified description of temperature-dependent hydrogen-bond rearrangements in liquid water, Proc. Natl. Acad. Sci. 102 (40) (2005) 14171–14174.
[54] B.M. Auer, J.L. Skinner, IR and Raman spectra of liquid water: theory and interpretation, J. Chem. Phys. 128 (2008) 224511–224512.
[55] B. Auer, R. Kumar, J.R. Schmidt, J.L. Skinner, Hydrogen bonding and Raman, IR, and 2D-IR spectroscopy of dilute HOD in liquid D_2O, Proc. Natl. Acad. Sci. 104 (36) (2007) 14215–14220.
[56] M.R. Waterland, D. Stockwell, A.M. Kelley, Symmetry breaking effects in NO_3: Raman spectra of nitrate salts and *ab initio* resonance Raman spectra of nitrate–water complexes, J. Chem. Phys. 114 (2001) 6249–6258.
[57] M. Xu, J.P. Larentzos, M. Roshdy, L.J. Criscenti, H.C. Allen, Aqueous divalent metal–nitrate interactions: hydration versus ion pairing, Phys. Chem. Chem. Phys. 10 (2008) 4793–4801.
[58] J.B. Matthew, F.M. Richards, The pH dependence of hydrogen exchange in proteins, J. Bio. Chem. 258 (5) (1983) 3039–3044.
[59] E. Canet, D. Mammoli, P. Kadeřávek, P. Pelupessy, G. Bodenhausen, Kinetic isotope effects for fast deuterium and proton exchange rates, Phys. Chem. Chem. Phys. 18 (15) (2016) 10144–10151.
[60] P.K. Glasoe, F.A. Long, Use of glass electrodes to measure acidities in deuterium oxide, J. Phys. Chem. 64 (1960) 188–190.